We are IntechOpen, the world's leading publisher of Open Access books Built by scientists, for scientists

4,800
Open access books available

122,000
International authors and editors

135M
Downloads

Our authors are among the

154
Countries delivered to

TOP 1%
most cited scientists

12.2%
Contributors from top 500 universities

WEB OF SCIENCE™

Selection of our books indexed in the Book Citation Index in Web of Science™ Core Collection (BKCI)

Interested in publishing with us?
Contact book.department@intechopen.com

Numbers displayed above are based on latest data collected.
For more information visit www.intechopen.com

Chapter 7

High-Resolution X-Ray Diffraction of III–V Semiconductor Thin Films

Hédi Fitouri, Mohamed Mourad Habchi and Ahmed Rebey

Additional information is available at the end of the chapter

http://dx.doi.org/10.5772/65404

Abstract

In this chapter, we will address the structural characterization of III–V semiconductor thin films by means of HRXRD. We first give an overview on the basic experimental apparatus and theory element of this method. Subsequently, we treat several examples in order to determine the effect of doping, composition and strain on structural properties of crystal. Analysed layers were grown by metal organic vapour phase epitaxy (MOVPE). Films treated as examples are selected in order to bring the utility of characterization technique. Here, we investigate GaAs/GaAs(001), GaAs:C/GaAs(001), GaN/Si(111), GaN:Si/Al_2O_3(001), GaAsBi/GaAs(001) and InGaAs/GaAs(001) heterostructures by using different scans for studying numerous structural layers and substrate parameters. Different scan geometries, such as ω-scan, $\omega/2\theta$-scan and map cartography, are manipulated to determine tilt, deformation and dislocation density induced by mismatch between layer and substrate. This mismatch is originated from the difference between the chemical properties of two materials generated by doping or alloying. Such HRXRD measurements are explored through the angular spacing between peaks of the substrate and layer. The half of full width maximum (HFWM) of peak layer intensity is a crucial qualitative parameter giving information on defect density in the layer.

Keywords: HRXRD, thin films, III–V semiconductors, alloys, stress, reciprocal map

1. Introduction

Over the past decade, the epitaxy of structures based on III–V materials has emerge to become of vital commercial importance within the electronics, optoelectronics and telecommunication industries. With rapid developments of epitaxy apparatus (such as molecular beam epitaxy or metal organic chemical vapour epitaxy) and *in situ* diagnostics (such as RHEED and

reflectometry), the elaborated active part of heterostructure has now come in the vicinity of idealism. However, such deviation from ideal properties (structural, optical or electrical) can reduce the device response. In this way and for economical reasons, it is desirable to characterize the as-grown layers prior to further processing. Indeed, high-resolution of X-ray diffraction (HRXRD) is now one of the widely used tools for non-invasive determination of the composition, thickness and perfection of the epitaxial layers of compound semiconductors. Recently, there had been great interest in the use of this technique with different scan geometries.

In this chapter, we will address the structural characterization of III–V semiconductor thin films by means of HRXRD. We first give an overview on the basic experimental apparatus of this method. Subsequently, we treat several examples in order to determine the effect of doping, composition and strain on structural properties of crystal.

2. Experimental details and theory element

All layers investigated in this work are elaborated by metal organic vapour phase epitaxy (MOVPE) technique [1–8].

For arsenide layers, we use a Bruker D8 diffractometer. An X-ray tube with a copper cathode generates the incident beam (1.54056 Å). In order to obtain highly monochromatic incident beam, we use a monochromator constituted by four Ge(022) crystals which gave a resolution of $\frac{\Delta\lambda}{\lambda} < 1.5\times10^{-4}$. The scattered beam can be detected by a scintillation point detector as reported in the left of **Figure 1**. The layer, that shall be examined, is mounted on the sample holder. As shown in the right of **Figure 1**, we denote ω as the angle between X-ray beam and the crystal surface, 2θ, the detector position, φ, the rotation angle around the normal of crystal and τ (or χ), the inclination angle of crystal in a perpendicular plane to the surface. This configuration gives a coupled and uncoupled scans, such as ω-scan (or rocking curve scan) and $\omega/2\theta$ scan.

For nitride layer, HRXRD measurements have been performed with a Bede 200 diffractometer equipped with a four-crystal monochromator in Si[220] mode.

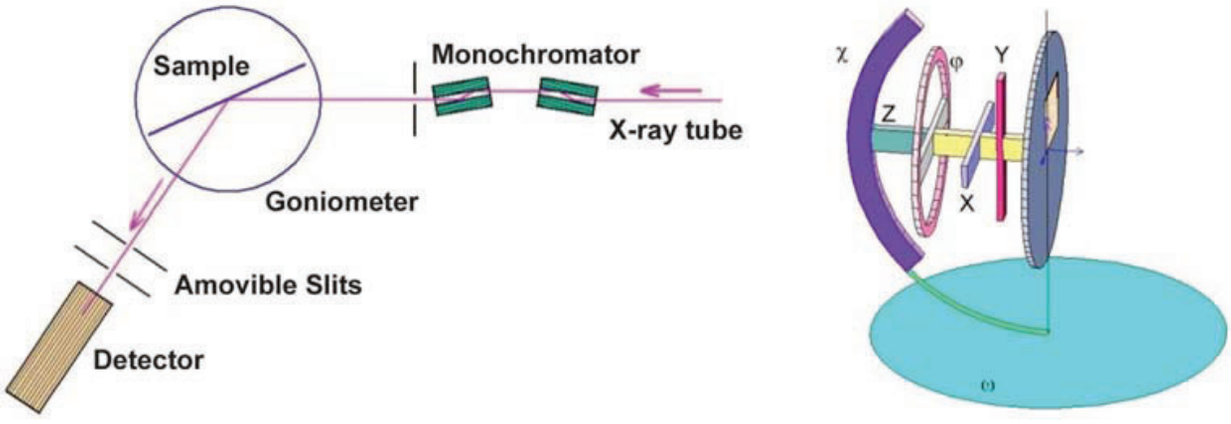

Figure 1. In the left, optical path of X-ray beam for the used goniometer. In the right, goniometer axes.

http://dx.doi.org/10.5772/65404

The simple form of Bragg equation for the lattice planes with Miller indices (*hkl*) and the distance d_{hkl} between two such adjacent planes is given by

$$2d_{hkl}\sin\theta = n\lambda \tag{1}$$

where:

- For cubic lattice with lattice constant a,$d_{hkl} = \frac{a}{\sqrt{h^2+k^2+l^2}}$,
- For hexagonal lattice with lattice constant a and c, $d_{hkl} = \frac{a}{\sqrt{\frac{4}{3}(h^2+k^2+hk)+(\frac{a}{c})l^2}}$.

Differentiation of Bragg equation and subsequent division of the result by the same equation yields the differential Bragg equation

$$\frac{\Delta d_{hkl}}{d_{hkl}} + \Delta\theta.\cot(\theta) = \frac{\Delta\lambda}{\lambda} \tag{2}$$

In our case, the spectral width of the incident beam is neglected ($\frac{\Delta\lambda}{\lambda}\sim 0$).

3. Application for thin films

3.1. Bulk films and substrates

Bulk substrates are characterized by a perfect crystallographic structure with an insignificant defect density. In HRXRD measurements, they have been used as a reference for Bragg angular measurements. But it is vital to minimize intrinsic and extrinsic effects, such as tilt substrate or tilt substrate-to-holder sample (due to inaccurate sample mounting).

As an example, in order to determine the disorientation of GaAs substrate, the (004) rocking curves peak angles (ω_S) were taken for some azimuthal angle φ as shown in **Figure 2**. As mentioned earlier, ω_S variation follows the relation: $\omega_s(004) = \langle\omega_s\rangle + A\cos(\varphi - \varphi_0)$.

where A is the tilt or the disorientation to the absolute crystallographic substrate orientation.

Similarly, $\chi(004) = \langle\chi\rangle + A\sin(\varphi - \varphi_0)$ or $\chi(004) = \langle\chi\rangle - A\sin(\varphi - \varphi_0)$.

The best fit of experimental data by expression reported below allows the values of $\langle\omega_s\rangle = 33.0308^\circ$ and $A = 0.472^\circ$. By using Bragg's law, we can measure the lattice parameter of GaAs substrate $a_s = \frac{2\lambda_{CuKa1}}{\sin\langle\omega_s\rangle} = 5.6526\mathring{A}$. The manufacturer indicates that this commercial substrate is exactly orientated to (001) with a tolerance of ±0.5° and the lattice parameter is of $5.6533\mathring{A}$ corresponding to a Bragg angle of 33.028°. The difference between the two Bragg angles represents an error of about 0.003°. Also, the value of tilt A is in the same order of the tolerance given by the substrate producer.

3.2. Homoepitaxy

Homoepitaxy is the growth of a layer on the substrate where the two materials have the same physical characteristics (Si/Si, GaAs/GaAs, etc.). Such a structure is characterized by small full-

width at half-maxima (FWHMs) of measured peaks when growth is perfectly optimized and no supplementary information is given about the layer properties.

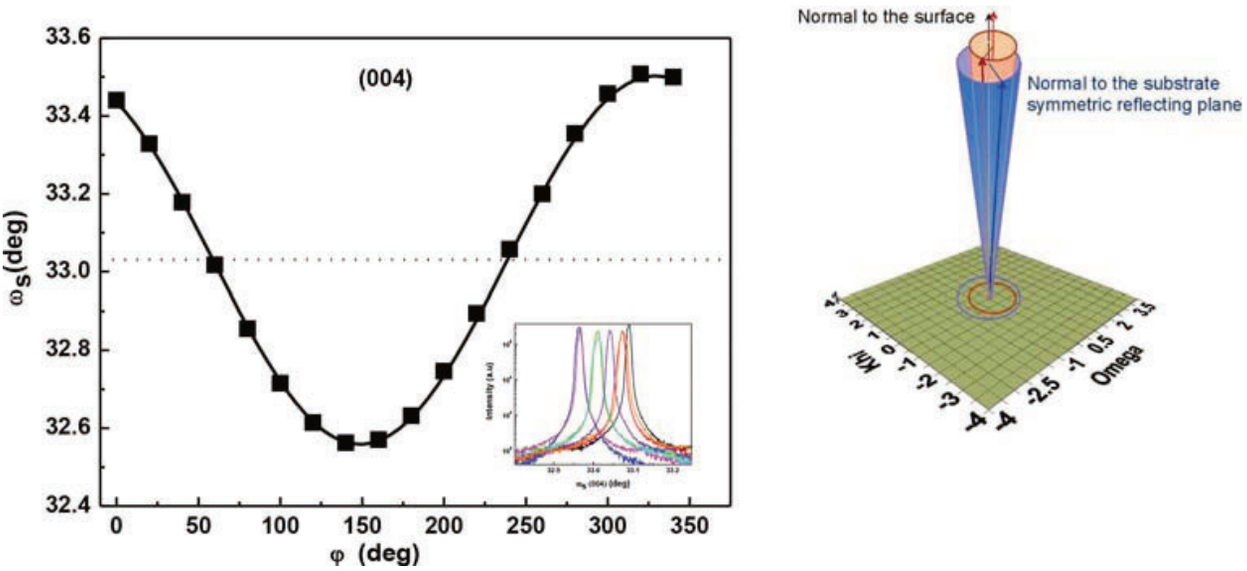

Figure 2. In the left, measured Bragg angle GaAs substrate of (004) rocking curves as a function of the azimuthal angle φ fitted by (the solid line) a sinusoidal equation. In the inset a series of rocking curves are shown. In the right, illustration of ω-scan around the normal to the substrate.

Doping of semiconductors is required to improve the electrical properties of material. In numerous applications, it is necessary to dope strongly n+ or p+ any part of the structure. Indeed, for tunnel effect or to obtain ohmic contact in GaAs, doping levels above 10^{19} cm^{-3} were needed. This requirement gives rise to a modification in structural properties of the doped layer. Yet, this deviation to ideal structure is clearly observed when atomic covalent radius of impurity is smaller or higher compared to atomic radius of matrix constituents. As an example, the doping of GaAs by carbon (C) gives rise to tetragonal distortion of GaAs caused by smaller covalent radius of C (r_c = 0.77 Å) compared to those of gallium (r_{Ga} = 1.26 Å) and arsenic (r_{As} = 1.20 Å). HRXRD is sensitive to this smaller deviation and will be used to determine the doping concentration.

The perpendicular lattice mismatch of C-doped GaAs was investigated by measuring (004) reflection and according to the following relation:

$$\varepsilon^{\perp} = \left(\frac{\Delta a}{a}\right)^{\perp} = -\Delta\theta_B \cot(\theta_B) \tag{3}$$

where $\theta_B = 33.028^\circ$ is the Bragg angle for (004) reflection.

On the other hand, in order to investigate the conditions of strain relaxation we have measured the parallel lattice mismatch $\Delta a_{//}$. Indeed, to find the in-plane lattice mismatch, an asymmetric (±1, ±1, ±5) reflection should be determined. The inclination angle φ is between a reflection from a lattice plane and the surface. The measurement of a reflection can be carried out at high

http://dx.doi.org/10.5772/65404

angle $\theta_B + \varphi$ or at a low angle $\theta_B - \varphi$. We can calculate the components of lattice mismatch from the measured differences in Bragg angle and lattice-plane orientation with regard to the substrate according to [9]:

$$\varepsilon^{\perp} = \frac{\Delta a^{\perp}}{a_{GaAs}} = \Delta\varphi tg\varphi - \Delta\theta \cot\theta_B \tag{4}$$

$$\varepsilon^{//} = \frac{\Delta a^{//}}{a_{GaAs}} = -\Delta\varphi \cot\varphi - \Delta\theta \cot\theta_B \tag{5}$$

In our case $\theta_B = 45.064°$ and $\varphi = 15.791°$.

For more details, let $\Delta\omega_a$ be the angular spacing between peaks of the substrate and of C-doped GaAs layer in $\omega/2\theta$ curve, and $\Delta\omega_b$ the same quantity measured after rotating the crystal by 180° around the normal to the wafer surface. Then, for (115) reflection

$$\Delta\varphi = \frac{1}{2}(\Delta\omega_a - \Delta\omega_b), \tag{6}$$

$$\Delta\theta_B = \frac{1}{2}(\Delta\omega_a + \Delta\omega_b). \tag{7}$$

The double determination of $\varepsilon^{\perp}$ from (004) and (115) reflections gives a more precision on its values than that of $\varepsilon^{//}$.

Based on this result, it is possible to determine the compensation ratio θ of our films using the Vegard's law in the strained form [10, 11].

$$\left(\frac{\Delta a^{\perp}}{a_{GaAs}}\right)_{strained} = \left(\frac{1+\upsilon}{1-\upsilon}\right)\left(\frac{\Delta a\perp}{a_{GaAs}}\right)_{relaxed} = 1.9\left(\frac{\Delta a\perp}{a_{GaAs}}\right)_{relaxed}. \tag{8}$$

We assume that the substituted carbon in the gallium site (C_{Ga} usually used to estimate the compensation) is the dominant cause of the compensation described by [12, 13]

$$\left(\frac{\Delta a^{\perp}}{a_{GaAs}}\right)_{relaxed} = \frac{4}{\sqrt{3}a_{GaAs}N}(\Delta r_{As} + \Theta\Delta r_{Ga})\frac{p_H}{(1-\Theta)} \tag{9}$$

where Δr_{As}= -0.43 Å and Δr_{Ga}= -0.49 Å are the difference between the covalent radii of C and As and Ga, respectively. $N = 2.22 \times 10^{22}$ cm^{-3} is the number of gallium or arsenic atoms per cm^3 in pure GaAs crystal and $\upsilon = 0.31$ is the Poisson's ratio.

Figure 3 illustrates a comparison between experimental data results and curves calculated for strained or relaxed states and with different compensation ratios. Using this dependence between $\frac{\Delta a^{\perp}}{a_{GaAs}}$ and p_H, we extrapolate the compensation ratio for any layer. We remark that the values deduced, using this consideration, are in the same order than that deduced by Hall Effect or SIMS measurements.

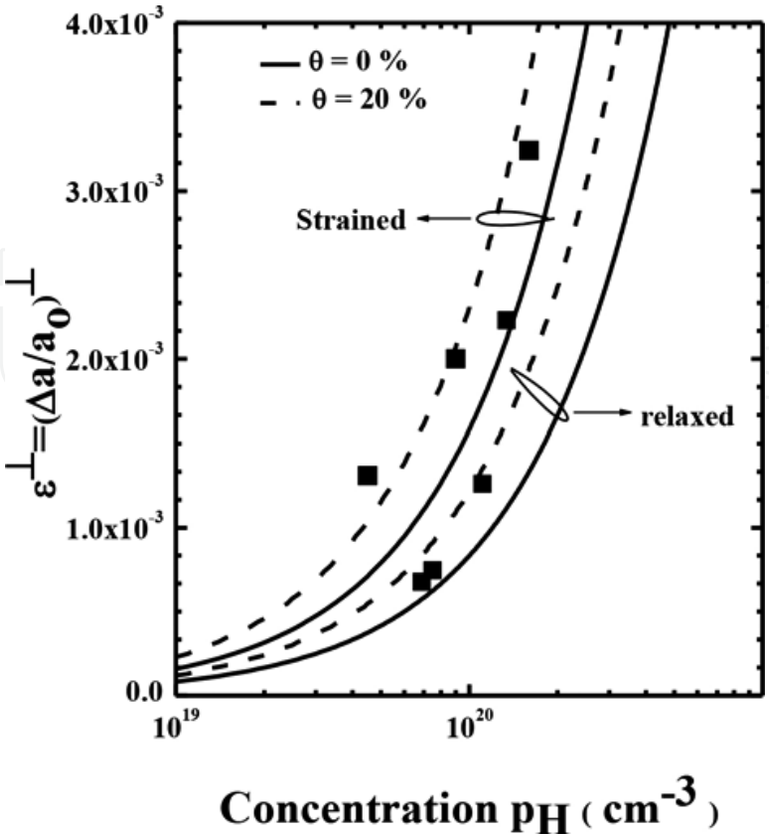

Figure 3. Perpendicular lattice mismatch ($\varepsilon^{\perp}$) of GaAs:C epilayers on GaAs substrates as a function of hole concentration p_H. The lines represent the predicted contraction based on Vegard's law for two values of compensation ratios $\theta = 0$ and $\theta = 0.25$.

3.3. Heteroepitaxy

Heteroepitaxy is the growth of a layer on the substrate where the two materials have different physical characteristics such as GaAs/Si, GaAs/Ge, GaN/Al_2O_3, etc. This means that the underlying substrate and the epitaxial layer are different materials with typically different lattice constants and perhaps even different crystal symmetry. Generally, this structure is characterized by misfit mismatch which generates stress and structural defects. In order to be accommodating to the substrate, the layer stays at less energetic equilibrium state which gives rise to appearance of tilt, twist and curvature of the system {layer + substrate}. HRXRD technique is able to determine these parameters.

3.3.1. Undoped GaN

III-Nitrides and related alloys cover a wide wavelength domain ranging from the red to the ultraviolet. Their interesting properties such as large and direct band gap make them attractive for the development of optoelectronic devices as well as high temperature and high power electronic applications. The MOVE growth of these materials is completed by using various substrates. However, the lack of suitable lattice matched substrate constitutes the major obstacle for further improvement in GaN material properties. Several attempts have been achieved for GaN growth on silicon substrate. Indeed, this choice is motivated by the availability with

low cost, the large size and high electrical and thermal conductivities of silicon. But, the success of GaN layer epitaxy requires a special growth procedure by using different processes (buffer layer, SiN treatment, etc.) in order to reduce the damage effects.

In this section, we focus on GaN layer grown on silicon substrate Si(111) where mismatch is of about 17%. This difference leads to the formation of a large number of defects (dislocations, cracks, etc.) and gives rise to layer mosaicity.

The GaN mosaicity can be usually described by two components of the misorientation: one is the tilt of *c*-axis with respect to the growth direction and the other is the twist of the columns orientation about the *c*-axis. GaN (00.l) ω-scans reflect the mosaic structure of the tilt among the crystallites. GaN (h0.l) ω-scans reflect the mosaic structure of twist between the crystallites. For symmetric (00.l) reflections, the full-width at half-maximum (FWHM) of the X-ray rocking curve (XRC) which characterize the tilt, was found to be around 1800 arcs. Note that both tilt and twist mosaics contribute to the rocking curve width of asymmetric (h0.l) reflections. For twist measurement, it is necessary to measure a series of reflections and extrapolate to an inclination angle χ of 90°. The plot of FWHM versus sin (χ) gives rise to an average twist of about 1.9° (**Figure 4**). The average twist was determined as half FWHM extrapolated to sin (χ) = 1. This high value of the twist can be explained by the interaction between hillocks of GaN during the nucleation process or dislocations which lead to a broad rocking curve width of GaN reflections.

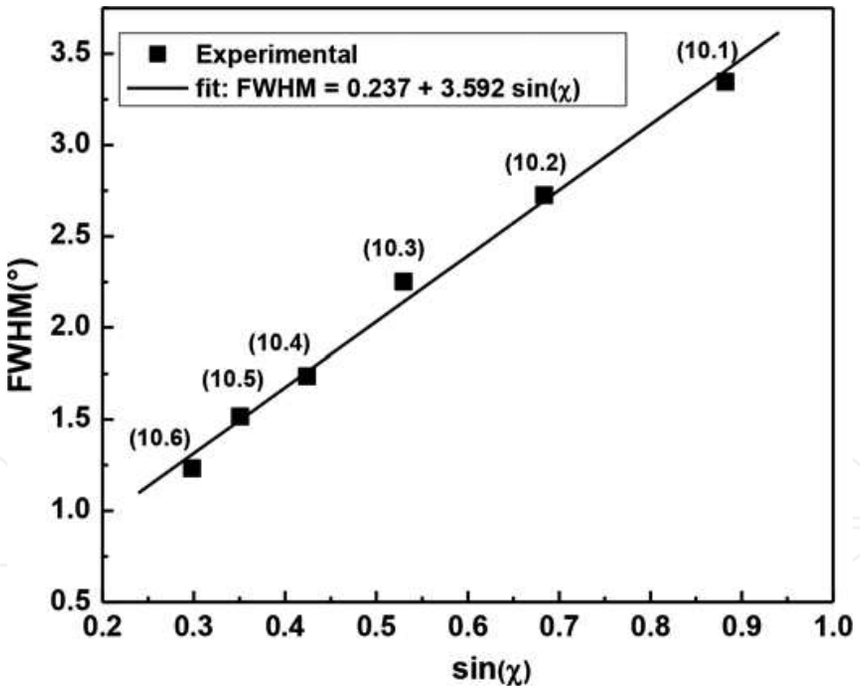

Figure 4. Evolution of FWHM (h0.l) plane reflections as a function of inclinations (χ) referring to (00.l) plane. The solid line represents the best linear fit of experimental data.

3.3.2. Si doped GaN

In order to study the effect of Si-doping on stress in GaN layers, HRXRD and Raman spectra measurements were carried out. **Figure 5** shows HRXRD patterns measured in $\theta/2\theta$ scan mode.

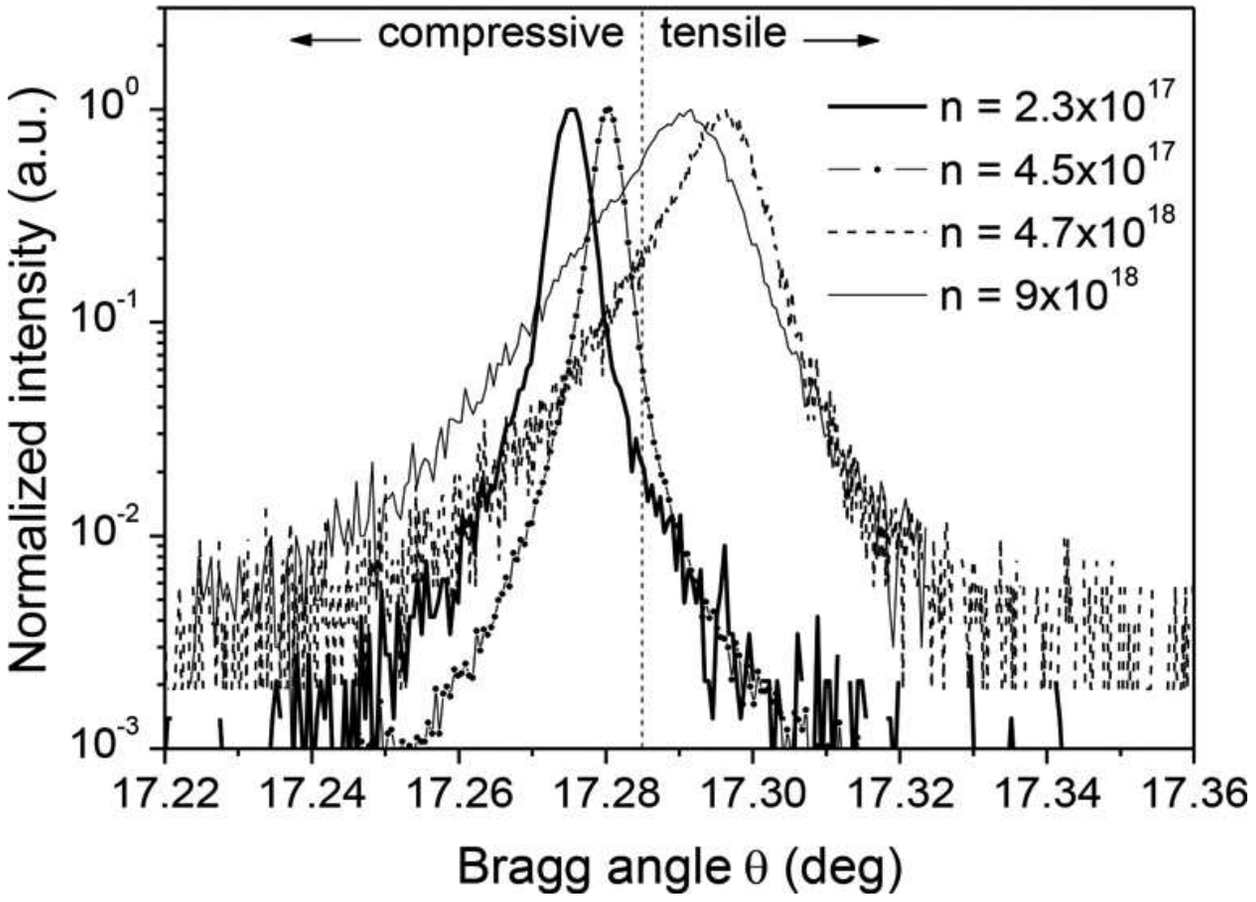

Figure 5. ω -scans of the Si-doped GaN samples.

The θ position shifts to the higher angle corresponding to smaller c lattice constant when Si concentration increases. The asymmetric shape of the ω-scan for high doping levels can be attributed to a stress gradient normal to the sample surface [14]. The in-plane stress $\sigma_{//}$ can be roughly determined from the relationships [15].

$$\sigma_{//} = \frac{a-a_0}{a_0}\left(C_{11} + C_{12} - 2\frac{C_{13}^2}{C_{33}}\right), \tag{10}$$

where C_{ij} are the elastic constants of GaN (C_{11} = 390 GPa, C_{12} = 145 GPa, C_{13} = 106 GPa, C_{33} = 398 GPa) [16]. a_0 is the lattice constant for strain-free bulk GaN (a_0 = 3.189 Å). The values of the a lattice parameter, measured by HRXRD, and the corresponding stress values $\sigma_{//}$ show that the incorporation of silicon not only leads to stress relaxation in GaN layers, but also induces tensile stress ($\sigma_{//} > 0$) for doping levels higher than 1.6×10^{18} cm^{-3}. According to our PL data analysis (not shown here), we attribute the strong band gap reduction in the Si-doped GaN layers is essentially due to the relaxation of stress in these layers.

The effect of silicon doping on the mechanism of stress relaxation and defect formation in GaN is still under discussion. One plausible explanation is that the relaxation increases with Si-induced defects formed during the cool-down process [17, 18]. Thus, we can assume that the incorporation of silicon leads to increase of the dislocation density in the GaN epilayer. Note that the dislocation densities in GaN-based materials have been generally measured by

transmission electron microscopy (TEM) and etch pit densities (EPDs). However, as non-destructive method, X-ray rocking curves (ω-scans) can be used to measure the dislocation densities with accuracy equal to TEM and EPDs. The theory elements of this technique are described by Gay et al. [19] and Hordon and Averbach [20], for the case of highly dislocated metal crystals and extended by Ayers [21] to the case of zinc-blende semiconductors.

The model developed by Ayers uses the rocking curve line width broadening owing to threading dislocations for calculation of their densities. Then, the square of the measured rocking curve line width β_m for the (*hkl*) reflection can be written as [21]:

$$\beta_m^2(hkl) = K_\alpha + K_\varepsilon \tan^2\theta \tag{11}$$

where $K_\alpha = 2\pi\ln(2b^2D)$, $K_\varepsilon = 0.09\, b^2D \mid \ln(210^{-7}cm\sqrt{D}|$, b is the length of the burgers vector and D is the dislocation density. K_α is the rocking curve broadening owing to angular rotation at dislocations. K_ε is the broadening produced by strain surrounding dislocations.

The plot of β_m^2 versus $\tan^2\theta$ should give rise to a straight line. The dislocation densities can be independently calculated from the slope (K_ε) as well as the intercept (K_α). The obtained results based on the two ways should be identical. A plot according to last equation for various X-ray peaks is shown in **Figure 6**. As predicted by the model, the symmetric and asymmetric reflections are on a single straight line. Dislocation densities calculated according the Ayers model from the slopes and intercepts of these linear fits are shown in **Figure 7**.

AFM data corresponding to the densities of surface depressions and pinned steps are also given for comparison. It is well known that the surfaces of GaN layers grown by MOVPE are typically dominated by these two kinds of dislocation mediated surface structures [22]. So, as seen in **Figure 7**, the dislocation densities calculated from the slopes (D_ε = 8.4 × 10^8 to 7.1 × 10^9 cm^{-2}) are in same order of magnitude with that obtained by AFM measurements (D_{AFM}=1.3 × 10^9 to 8 × 10^9 cm^{-2}). The lack of internal consistency (D_ε slightly different from D_α) may be explained by the existence of sources of rocking curve broadening other than dislocations that give rise to different relative amounts of rotational and strain broadening [21].

3.4. Alloys

The III–V materials have raised a fundamental attention in the field of optoelectronics and rapid electronics. Particularly, the alloy semiconductors have an exceptional amount of interests owing to the possible adjustment of band gap and lattice parameter by changing chemical composition. Recently, the technological progress of elaboration and process techniques provides a great opportunity to design new structure architecture and quantum nanostructure based on non-conventional semiconductor materials. This fact requires a suitability of characterization tools adapted to this advance.

3.4.1. GaAsBi alloy as a new material

Owing to the large size and core electronic structure of Bi atom, Bi-containing semiconductor alloy materials exhibit a small or negative band gap. The interesting properties of III–V-Bi alloy offer a great opportunity for possible design in optoelectronic application devices. Recent

results from various groups demonstrated that $GaAs_{1-x}Bi_x$ thin films can be produced by molecular beam epitaxy (MBE) [23–25] or by MOVPE [1, 2, 26–28]. Further, $GaAs_{1-x}Bi_x$ alloy presents temperature insensitivity of band gap required in the resolution of problems of the lasing wavelength fluctuations. The quality of epitaxial compound film is governed by thickness uniformity, degree of alloying and substrate temperature. Precisely, the growth behaviour of $GaAs_{1-x}Bi_x$ was quite different from that of usual ternary semiconductor alloys such as GaInAs and AlGaAs. A very narrow growth conditions are reported by comparison between structural and optical characterizations. In this way, HRXRD is comely tool to investigate the structural properties of this material.

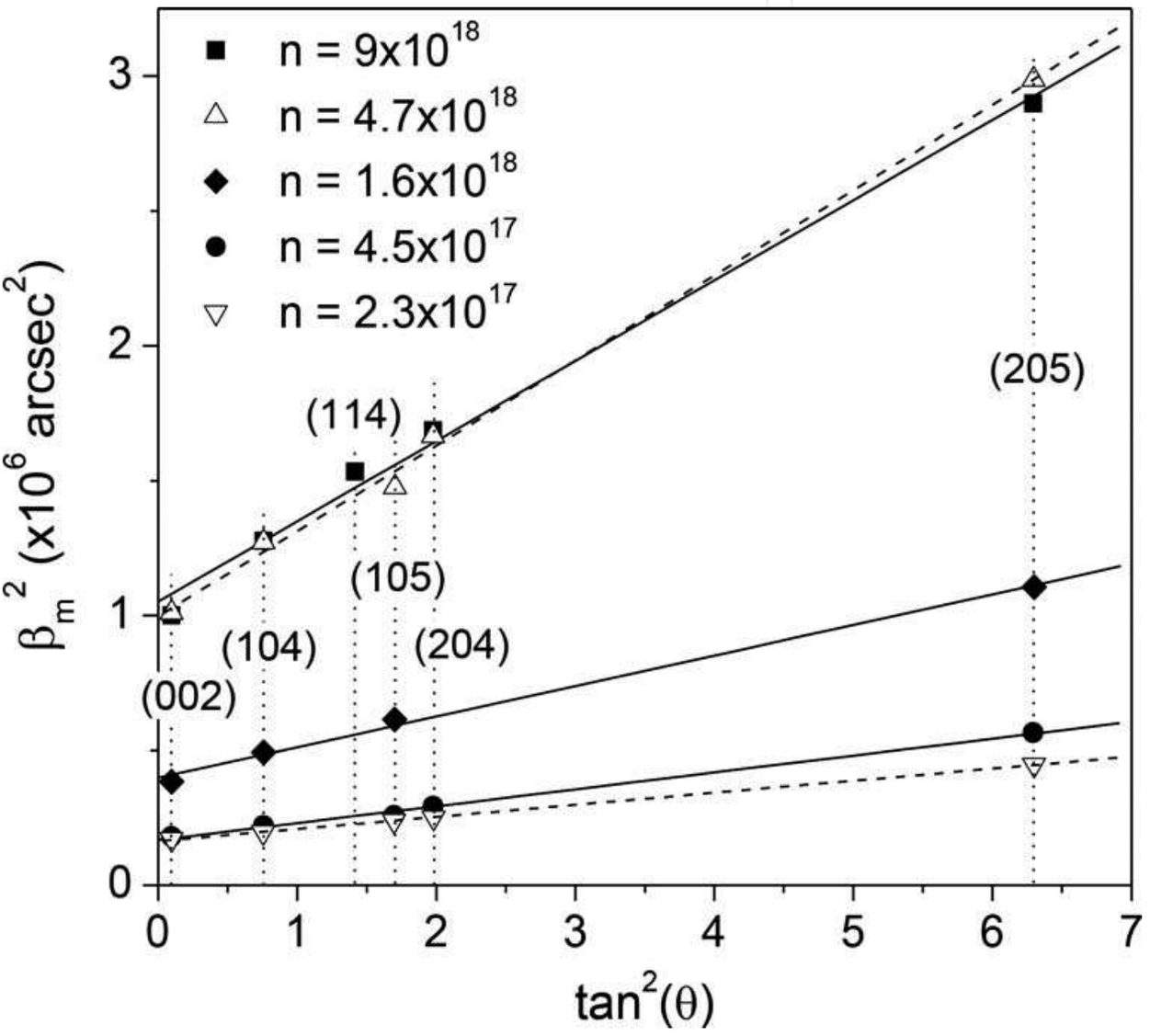

Figure 6. Square of rocking curve line width β_m (*hkl*) versus $\tan^2\theta$ for Si-doped GaN samples.

Figure 8 shows the diffraction pattern in the θ –2θ scan of X-ray diffraction measurement for a $GaAs_{1-x}Bi_x$ layer grown on p-type GaAs substrate. The spectrum shows three resolved peaks located at 31.627, 66.048 and 65.528° which are associated with the plane diffraction of (002)

http://dx.doi.org/10.5772/65404

and (004) GaAs and (004) $GaAs_{1-x}Bi_x$, respectively (detail is shown in the inset figure). No other phases were identified.

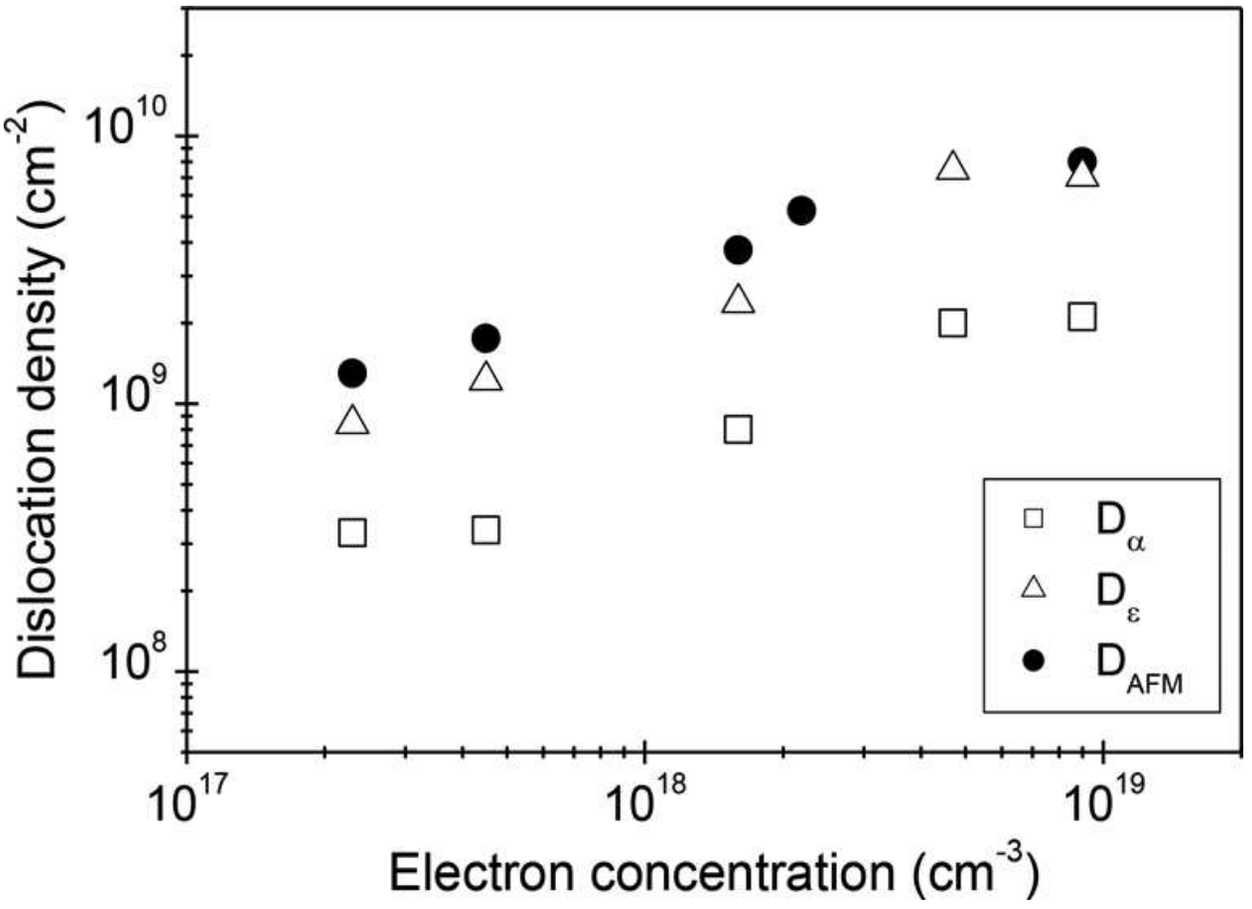

Figure 7. Dislocation densities calculated according to Ayers model from slopes (D_ε) and intercepts (D_α). AFM data are given for comparison.

HRXRD measurements of symmetric (004) and asymmetric (115) plane diffractions were carried out in order to determine the lattice parameter of $GaAs_{1-x}Bi_x$ and then Bi composition, as shown in **Figure 9**. In fact, the presence of two peaks relative to the layer and substrate diffractions, Pendellösung oscillations, seen in the wings of peaks, reveals a smooth and coherent interface. From these oscillations, we can calculate the layer thickness from Bragg's law: $t = \frac{\lambda \gamma_H}{\Delta\omega \sin(2\theta_B)}$. The period ($\Delta\omega$) is independent of scattering power of layer composition. $2\theta_B$ is the scattering angle, λ is the wavelength of the X-ray radiation and $\gamma_H = \sin(\theta_B + \varphi)$. φ is the angle between the diffraction planes and the surface.

The lattice constants in growth direction ($a_\perp$) and in the plane ($a_{//}$) of $GaAs_{1-x}Bi_x$ layer were calculated from the peak separation ($\Delta\theta_B$) between GaAs and $GaAs_{1-x}Bi_x$. $a_\perp$ is deduced from the spacing of the layer (004) plane (d_{004}) in the form of $a_\perp = 4\ d_{004}$ using a symmetric reflection (004). From asymmetric reflection (115), $a_{//}$ is deduced from the spacing of the layer (115) plane (d_{115}), in the form of $a_{//} = \sqrt{2}\left[\frac{1}{d_{115}^2} - \frac{25}{a_\perp^2}\right]^{\left(-\frac{1}{2}\right)}$.

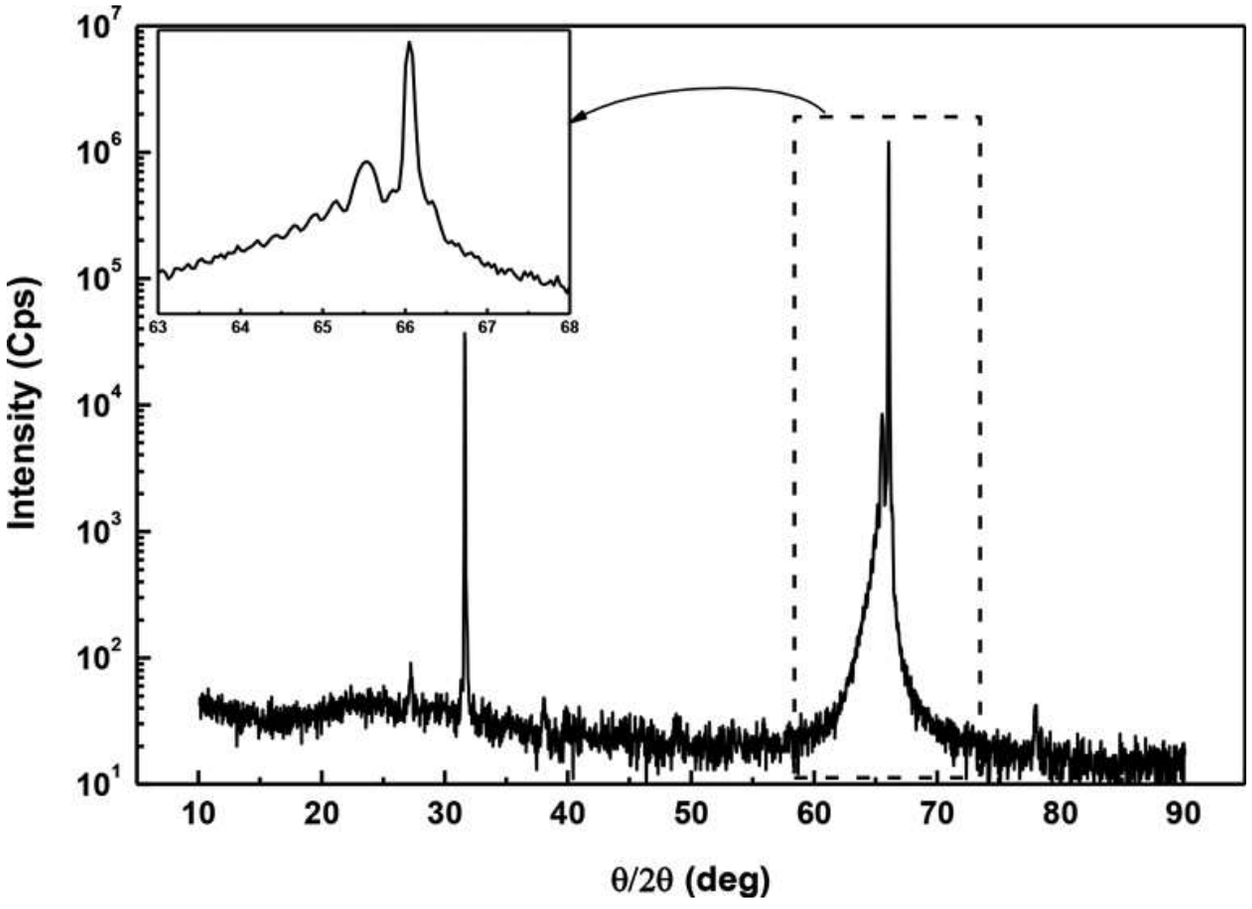

Figure 8. Diffraction pattern in the θ –2θ scan of X-ray diffraction measurement for a $GaAs_{1-x}Bi_x$ layer grown on (100) Zn doped GaAs substrate. The inset shows a zoom between $2\theta = 63^\circ$ and 68°.

The lattice constant (a_0) of unstrained cubic $GaAs_{1-x}Bi_x$ is assumed from

$$a_\perp = a_{//} + (a_0 - a_{//}) \frac{(C_{11} + 2C_{12})}{C_{11}} \tag{12}$$

where $C_{11} = 11.92$ and $C_{12} = 5.99$ are the elastic constants for $GaAs_{1-x}Bi_x$ which are supposed to be equal to those of GaAs. The Bi composition x, is calculated from a_0 using Vegard's law:

$$a_0 = x a_{GaBi} + (1-x) a_{GaAs} \tag{13}$$

where a_{GaBi} is the lattice constant of hypothetical zinc-blend GaBi and assumed to be 6.324 Å [29]. a_{GaAs}= 5.653 Å is the lattice constant of GaAs.

Thickness homogeneity and layer composition were characterized by recording (004) X-ray $\omega/2\theta$ curves for several positions in the layer surface. Small changes of 0.001 and 0.002° mm^{-1} have been detected for $\Delta\omega$ and $\Delta\theta_B$, respectively. Bi composition is estimated to 3.7% with a relative change of about 0.05% per mm. The layer thickness is about 50 nm. These values were also compared to those deduced from simulated X-ray patterns using the dynamical theory

http://dx.doi.org/10.5772/65404

shown as dotted lines in **Figure 9**. The tetragonal distortion induced by the epitaxy is taken into account using the elastic constants of GaAs.

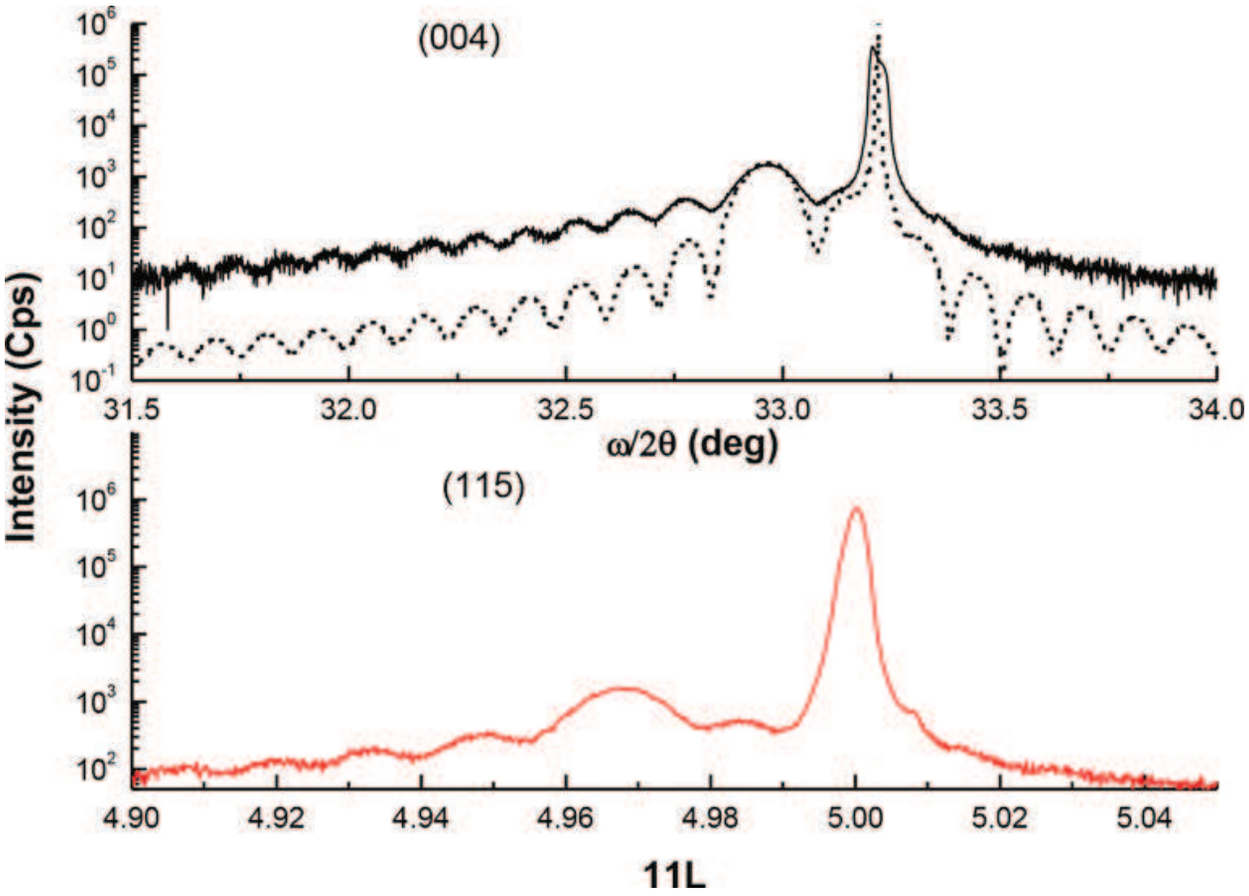

Figure 9. In the top: HRXRD (004) experimental $\omega/2\theta$ curve (solid line) and simulated curve (dotted line) of $GaAs_{0.963}Bi_{0.37}$ layer grown on (100) Zn doped GaAs substrate. In the bottom: optimized scan of HRXRD (11L) reflection plane. L is changed around 5.

The optimization of GaAsBi MOVPE growth conditions was detailed in our previous works [1, 2]. A good crystalline quality was obtained using a V/III ratio of about 9.5, trimethylbismuth (TMBi) flow of 0.2 μmol min^{-1} and a growth temperature of 420°C. The measured Bi content value is around 3.7%. The epitaxial layers show a low Bi island density on the surface [2]. It should be noted that small deviations from optimal growth conditions may give rise to a surface formation of big Bi droplets. The latter appear with a higher density and different shapes for high TMBi flow (~3 μmol min^{-1}).

As a demonstrative example, **Figure 10** illustrates the diffraction patterns of symmetric (004) and asymmetric (115) reflections for the as-grown and annealed GaAsBi layers grown with high TMBi flow. To check thermal stability, GaAsBi layer was annealed at 750°C for 15 min under AsH_3 flow. These curves present more diffraction peaks, other than that of the GaAs substrate, located at 32.8, 32.5 and 32.12° in the left side of the substrate peak, and denoted as GaAsBi(1), GaAsBi(2) and GaAsBi(3), respectively. The same diffraction peaks have been detected in the (115) asymmetric configuration, but more shifted with respect to GaAs

substrate peak. It seems that these three peaks are linked to different Bi contents in GaAsBi layer. Based on the Vegard's law we have found: $x_{GaAsBi(1)}$ = 3.7%, $x_{GaAsBi(2)}$ = 8% and $x_{GaAsBi(3)}$ = 14%. The obtained Bi contents are calculated after the determination of the lattice constants perpendicular and parallel to GaAsBi surface using HRXRD measurements for the (004) and (115) planes, respectively. For hypothetical zinc blend GaBi, the lattice constant is estimated to be 6.324 Å [29]. More calculations details of Bi content are reported in the following Ref. [1]. We have also investigated the structural properties of the annealed layer at 750°C using HRXRD. The measured diffraction curves show a remarkable stability versus thermal annealing. In fact, the same curve shape was obtained for annealed sample (**Figure 10**). Bi droplets are entirely removed from GaAsBi layer after annealing. This behaviour shows that the existence of these droplets is not responsible of diffraction peaks appearance and confirms the structural thermal stability of GaAsBi alloy (**Figure 10**).

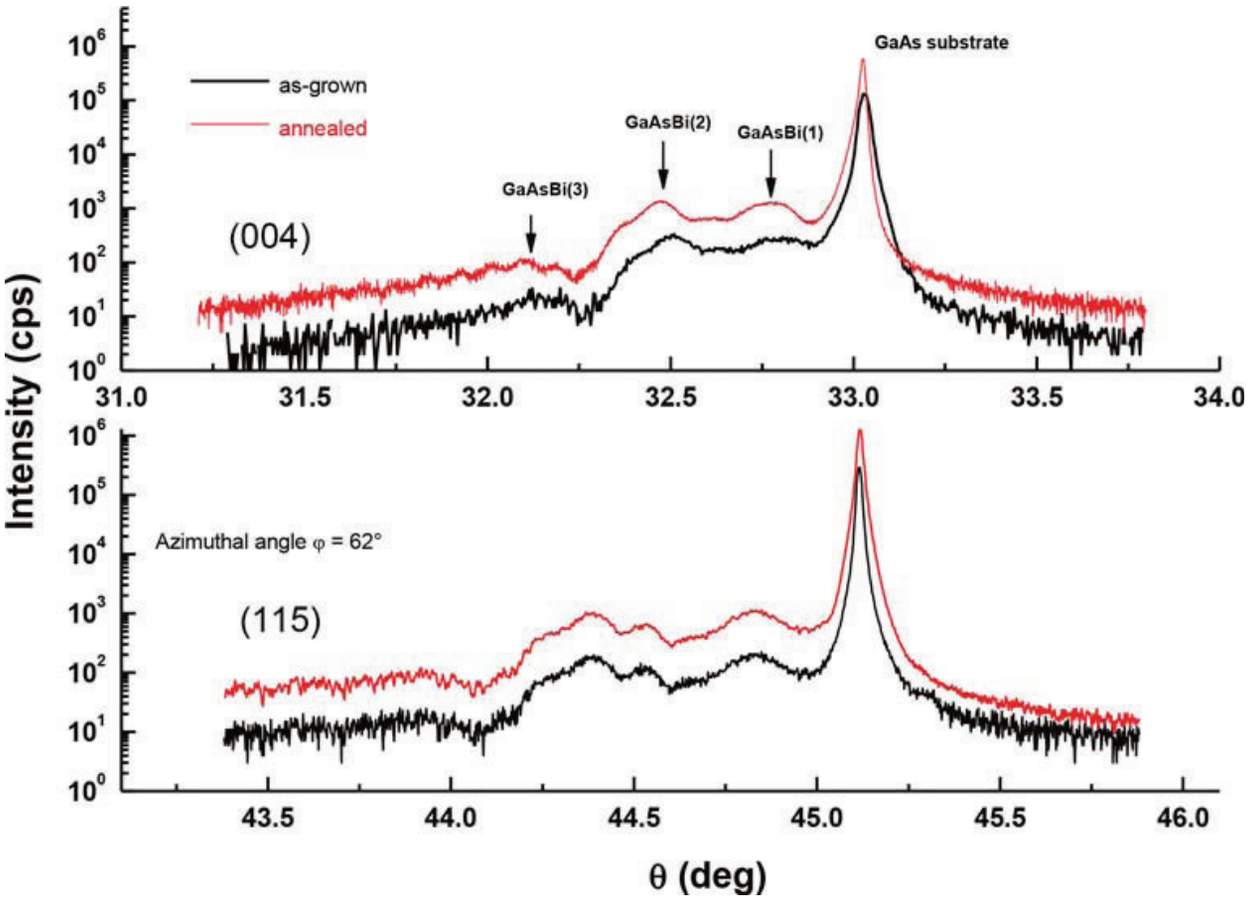

Figure 10. HRXRD (004) and (115) experimental $\omega/2\theta$ patterns of as-grown and annealed GaAsBi layers grown on GaAs substrate at 420°C under 3 μmol min^{-1} of TMBi flow.

To find out an eventual crystallographic tilting of this sample, we have achieved several ω scans for different azimuthal angles φ for each resolved peak indicated by arrows and shown in **Figure 11**. We report in **Figure 11**, for different azimuthal angles, the diffraction angles variation of the substrate $\omega_{Substrate}$ and the layer ω_{GaAsBi} for the three aforementioned peaks (GaAsBi(1), GaAsBi(2) and GaAsBi(3)). All the measured amplitudes of the cosine variation of

http://dx.doi.org/10.5772/65404

$\omega_{Substrate}$ and ω_{GaAsBi} are about 1.18°. Note that the given incertitude on GaAs substrate off cut angle is about 1°, and then the GaAsBi layer is not tilted with respect to the substrate. The splitting between the farthest GaAsBi(004) multiple diffraction peaks is about 0.68°. This value is probably corresponding to a maximum tilt between GaAsBi grains which can be present in the layer.

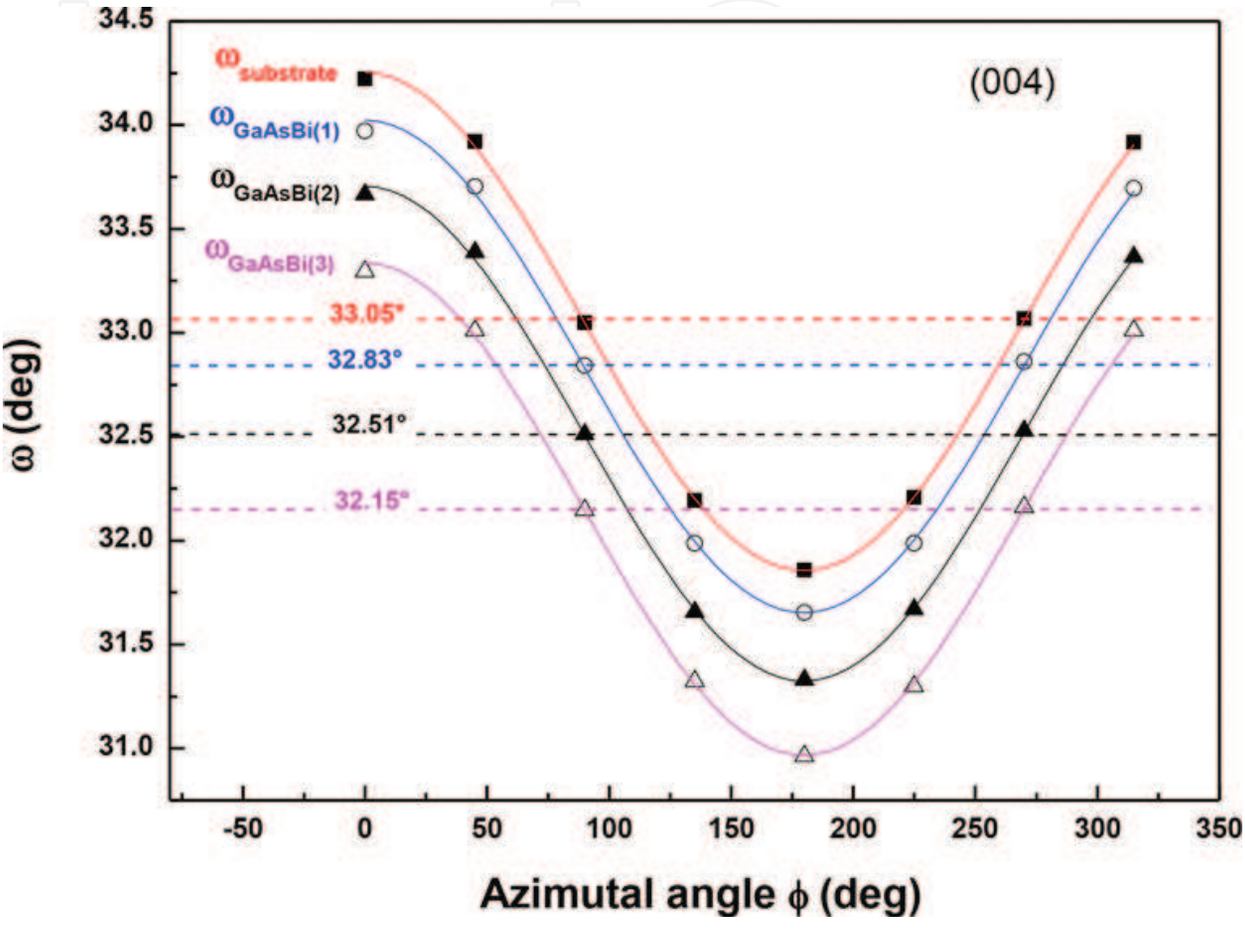

Figure 11. Diffraction angles variation of GaAs substrate (ω_S) and GaAsBi layer (ω_L) for the three aforementioned peaks versus azimuthal angles φ.

Ciatto et al. [30] have investigated the local structure around Bi atoms in GaAsBi layers. Their X-ray absorption spectrometry results show that at 1.2% Bi content, Bi atoms are randomly distributed. At 1.9%, Bi atoms tend to form next-nearest-neighbour pairs, and at 2.4% Bi aggregates appear. In our work, the lowest Bi content in GaAsBi layer is around 3.7%, showing that necessarily Bi aggregates are already formed in the layer.

X-ray diffraction measurements exhibit that growth under high TMBi flow leads to a compositional inhomogeneity, as well as the presence of liquid can affect the Bi incorporation. This fact may be responsible of the XRD pendellösung fringes vanishing, and it was clearly seen when growing GaAsBi under optimized conditions [1, 2]. Some caution is required when interpreting X-ray profile of GaAsBi layers. The confusion can arise from metallic Bi diffraction peak, which can appear in layers having Bi droplet on the surface. Since thermal annealing at

750°C have completely removed Bi islands from the surface, and diffraction curve are exactly the same as before annealing, so this confirms that metallic Bi does not contribute to the diffraction curve.

On interpreting our X-ray profile, the probable assumption is the presence of atomic disorder created by Bi during its incorporation in GaAs matrix. Indeed, the disorder becomes more significant with increasing Bi content. In our case, this content is higher than 3.7% which explains the important disorder and the appearance of several diffraction peaks. There are some assumptions, like support phase separation in GaAsBi alloy [27], the presence of 'micro regions' with different Bi contents [31] or a difference in the strain state at different depths [32].

3.4.2. InGaAs alloys

The lattice mismatch between GaAs and InGaAs alloy layers is relatively small which allows pseudomorphic growth to take place. But uppermost layer can also be partially relaxed or completely relaxed depending on the layer thickness and the indium composition. For a quantitative analysis, the degree of relaxation is given by

$$R = \frac{a_{\text{film}} - a_{\text{substrate}}}{a_{\text{film}}^{\text{relax}} - a_{\text{substrate}}} \tag{14}$$

where a_{film} denotes the measured lattice constant of the film and the totally relaxed lattice constant.R is equal to 1 for fully relaxed films and equal to 0 for pseudomorphic growth.

In this part, we explore a reciprocal space map (RSM) in order to investigate some structural properties of prototype InGaAs alloys in relaxed or strained states.

The Bragg equation relates every X-ray reflex that can be detected with a set of parallel lattice plane (hkl). However, the Laue condition attributes every X-ray reflex to reciprocal lattice point which makes it appropriate to label the reflexes with the indices of their corresponding reciprocal lattice points HKL. The maximum length of the scattering vector in the case of backscattering ($\theta_B = 90°$) is given by $Q_{\max} = 2|k| = \frac{4\pi}{\lambda}$.

Whenever the scattering vector is equal to reciprocal lattice vector, an X-ray reflex is observed. As a result, all reflexes which for a given wavelength λ are accessible for diffraction experiments are situated within the hemisphere with radius equal to $\frac{4\pi}{\lambda}$ (in right of **Figure 12**).

Such a scan can be carried out by combining the $\omega/2\theta$-scan with ω-scan mode in the following way: first for a given length of the scattering angle a ω-scan is accomplished, then the $\omega/2\theta$-scan mode is employed to change the length of the scattering vector by a small amount and then again a ω-scan is performed and shown as reported in left of the **Figure 12**. With RSM measurement, the graph can be presented either in angular coordinates or in reciprocal lattice coordinates. Angular coordinates RSM is the x- and z-axes can be ω, 2θ, $\omega/2\theta$, or $2\theta/\omega$. Reciprocal coordinates RSM shows the graph in reciprocal lattice unit Q_x and Q_z, where can be defined with the following equations [33]:

http://dx.doi.org/10.5772/65404

$$Q_Z = \frac{2}{\lambda}\sin\theta\cos(\omega-\theta)$$
$$Q_X = \frac{2}{\lambda}\sin\theta\sin(\omega-\theta) \quad (15)$$

where λ = 1.5406 Å is the wavelength of $CuK_{\alpha 1}$ radiation, $\theta = 2\theta/2$ the angular position of the detector and ω is the experimental Bragg angle for considered reflection.

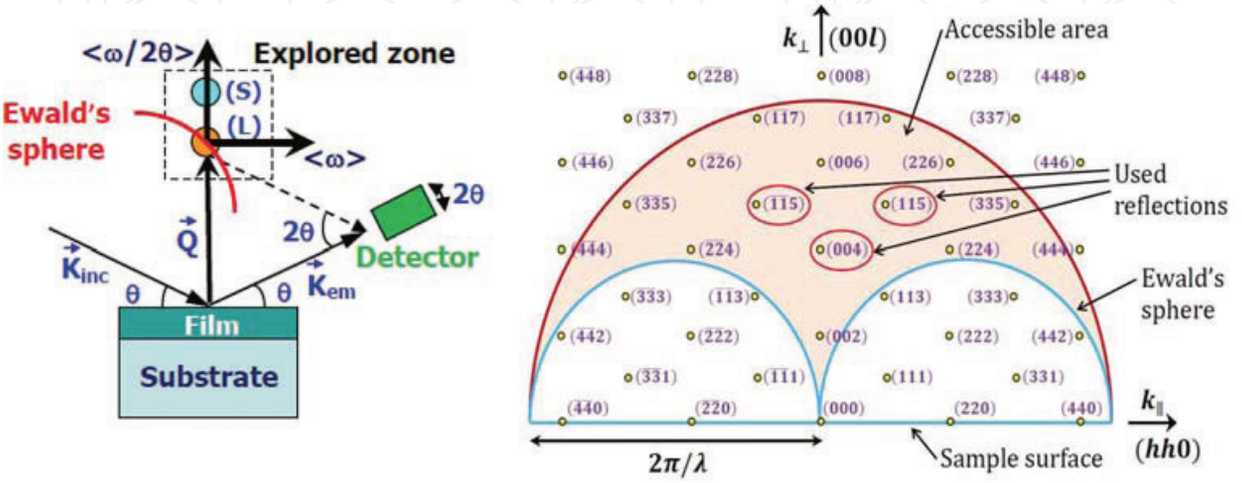

Figure 12. Ewald construction illustrating the scattering geometry in the cases of symmetrical and asymmetrical reflexes. The grey arrows show the scan directions for $\omega/2\theta$-scan and a ω-scan. The accessible reflections in conventional scattering geometry are shown.

ΔQ_Z and ΔQ_X are determined from the difference between measured angles for the substrate and the layer. For (115) reflection on (001) substrate, the perpendicular lattice parameter of the layer is obtained from $\Delta Q_Z = \frac{5}{a_\perp} - \frac{5}{a_s}$
where a_{GaAs}=5.6325 Å is the lattice parameter of the GaAs substrate.

Other possible equivalent representations of reciprocal map are accessible, such as by that representing the Bragg angle change by changing (*hkl*) indices.

Generally, the reciprocal maps show two intense peaks localized in $\Delta Q_X = \Delta Q_Z = 0$ relative to the GaAs substrate and the in $\Delta Q_X \neq \Delta Q_Z \neq 0$ relative to the layer.

3.4.2.1. InGaAs/GaAs relaxed layer

Figure 13 illustrates an example of 2D and 3D map representations for a sample InGaAs/GaAs. In order to analyse maps topography with more facility, pedagogic representation as contour curves of iso-intensity is reported in the same figure.

Using RSM, the analysis of material properties can be completed both qualitatively and quantitatively. The last figure shows the illustration of a qualitative description of the change of the layer peak position with respect to the substrate peak. Qualitatively, a symmetric RSM scan can confirm that our sample is tilted or not. However, to determine whether our sample is strained or relaxed, an asymmetric scan is needed.

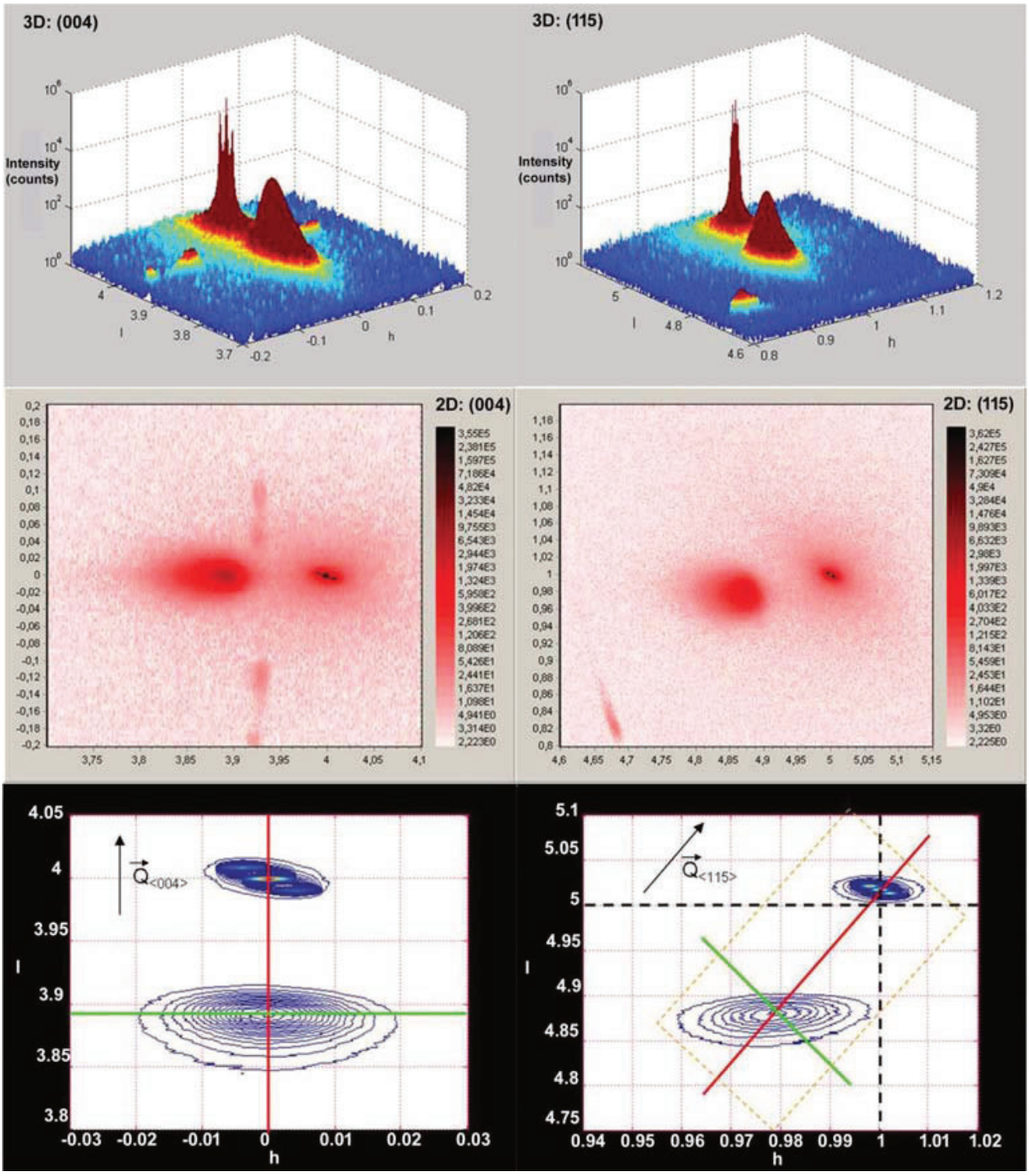

Figure 13. 3D and 2D reciprocal space maps of $In_{.08}Ga_{.92}As/GaAs$ structure, recorded around (004) and (115) nodes. In the bottom, contour curves of iso-intensity are drawn. Diffusion vectors $\vec{Q}_{(004)}$ and $\vec{Q}_{(115)}$ were added to corresponding RSM.

3.4.2.2. InGaAs/GaAs strained layer

InGaAs epitaxial layer on GaAs(100) substrate was investigated by HRXRD in order to determine the structural properties of this strained structure. **Figure 14** shows reciprocal space

http://dx.doi.org/10.5772/65404

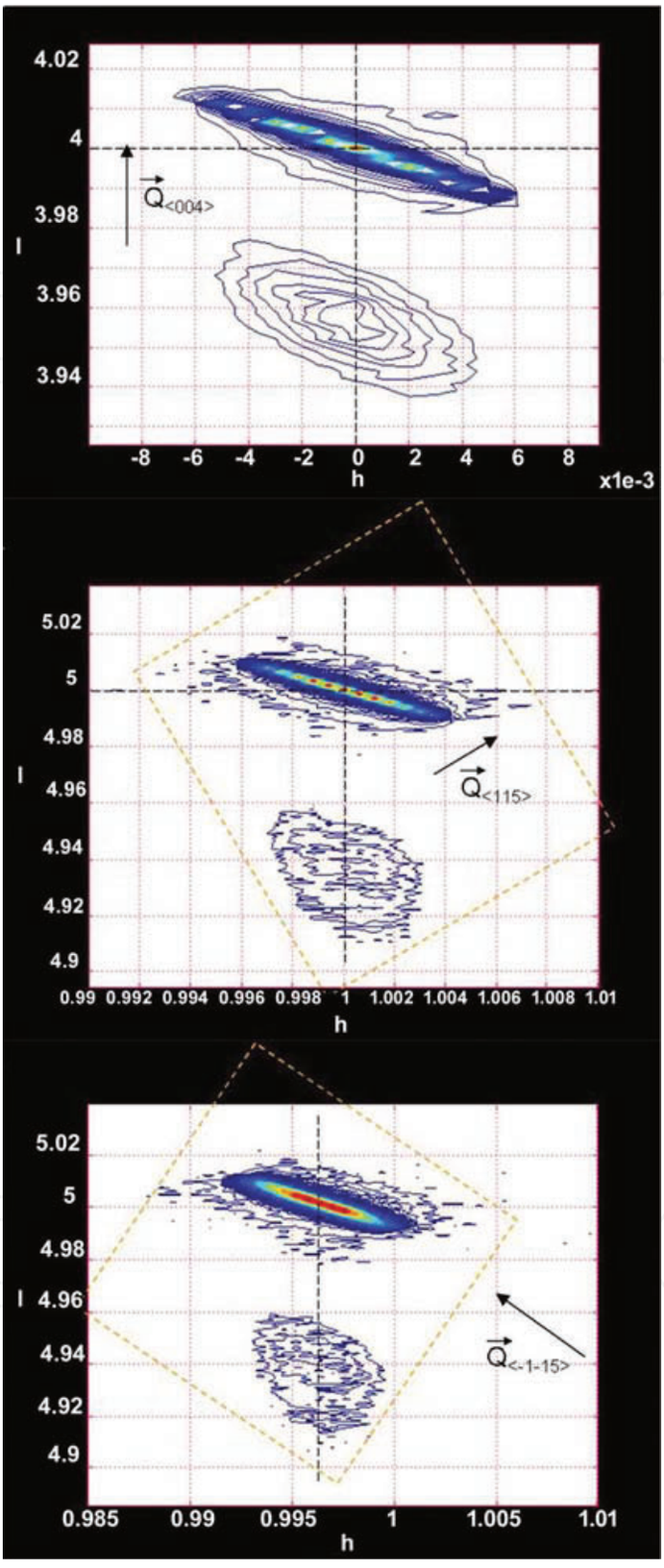

Figure 14. Reciprocal space mapping of $In_{.08}Ga_{.92}As/GaAs$ structure, recorded around (004), (115) and $(\overline{1\bar{1}5})$ nodes. Diffusion vector $\vec{Q}_{(hhl)}$ was added to the corresponding RSM.

maps (RSM) of an InGaAs/GaAs sample in two-dimensional representation of iso-intensity curves around (004), (115) and $(\overline{1\overline{1}5})$ nodes. Note that both spots of InGaAs active layer and GaAs substrate, relative to (004) symmetric reflection, were aligned along <001> direction. The obtained result confirms the absence of tilt between the active layer and the substrate. In addition, diffraction spots from (115) and $(\overline{1\overline{1}5})$ asymmetric reflections were also aligned along the growth direction, which was different from that of scattering vector $\vec{Q}$. Sample was then strained and pseudomorphed. A fully strained epilayer adapts its planar lattice fully with the planar lattice of the substrate (**Figure 14**).

4. Conclusions

This chapter has covered a range of applications of HRXRD technique from simple rocking curve scans (ω and $\omega/2\theta$) to space mapping cartography. Routine measurements applied to particular heterostructures such as GaAs/GaAs(001), GaN/Si(111), GaAsBi/GaAs(001) and InGaAs/GaAs(001) are reported in order to bring the capability of analysis of this technique. The former is a powerful tool that can provide accurate information on the structural properties of the analysed material. Indeed, the method is sensitive enough to determine the composition, thickness and perfection of the epitaxial layers of compound semiconductors.

The application of high-resolution diffraction space mapping is more prevalent since it is now possible to obtain a whole wealth of structural parameters other than just the thickness or composition. This is a developing field and this technique can be considered to determine the deviation from perfection.

Acknowledgements

The authors would like to acknowledge all URHEA members, particularly, Mrs B. El Jani, N. Chaaben, A. Bchetnia and C. Bilel for their help in HRXRD measurements.

Author details

Hédi Fitouri, Mohamed Mourad Habchi and Ahmed Rebey*

*Address all correspondence to: ahmed.rebey@fsm.rnu.tn

Faculty of Sciences, Research Unit on Hetero-Epitaxy and Applications, University of Monastir, Monastir, Tunisia

References

[1] H. Fitouri, I. Moussa, A. Rebey, A. Fouzri, B. El Jani, J. Cryst. Growth 295 (2006), 114–118.

[2] I. Moussa, H. Fitouri, A. Rebey, B. El Jani, Thin Solid Films 516 (2008), 8372–8376.

[3] M. M. Habchi, A. Rebey, B. El Jani, J. Cryst. Growth 310 (2008), 5259–5265.

[4] M. M. Habchi, A. Rebey, B. El Jani, Microelect. J. 39 (2008), 1587–1593.

[5] A. Rebey, L. Béji, B. El Jani, P. Gibart, J. Cryst. Growth 191 (1998), 734–739.

[6] A. Rebey, B. El Jani, A. Leycuras, S. Laugt, P. Gibart, Appl. Phys. 68 (1999), 349–352.

[7] A. Bchetnia, A. Touré, T.A. Lafford, Z. Benzarti, I. Halidou, M.M. Habchi, B. El Jani, J. Cryst. Growth 310 (2008), 5259–5265.

[8] N. Chaaben, T. Boufaden, A. Fouzri, M.S. Bergaoui, B. El Jani, Appl. Surf. Sci. 253 (2006), 241–245.

[9] X. R. Wang, X. Y. Chi, H. Zheng, Z. L. Miao, J. Wang, Z. S. Zhang, Y. S. Jin. J, Vac. Sci. Technol. B 6(1) (1988), 34.

[10] N. Chen, Y. Wang, H. He, L. Lin, Phys. Rev. B. 54(12) (1996), 8516.

[11] W. Lei, M. Pessa, Phys. Rev. B 57(23) (1997), 14627.

[12] A. Rebey, W. Fathallah, B. El Jani, Microelect. J. 37 (2006), 158–166.

[13] A. Rebey, Z. Chine, W. Fathallah, B. El Jani, E. Goovaerts, S. Laugt, Microelect. J. 35 (2004), 875–880.

[14] A. Cremades, L. Görgens, O. Ambacher, M. Stutzmann F. Scholz, Phys. Rev. B 61 (2000), 2812.

[15] V. S. Harutyunyan, A. P. Aivazyan, E. R. Weber, Y. Kim, Y. Park S. G. Subramanya, J. Phys. D: Appl. Phys. 34 (2001), A35–A39.

[16] A. Polian, M. Grimsditcv, I. G. Grzegory, J. Appl. Phys. 79 (1996), 3343.

[17] Z. Chine, A. Rebey, H. Touati, E. Goovaerts, M. Oueslati, B. El Jani, S. Laugt, Phys. Stat. Sol. (A) 203(8) (2006), 1954–1961.

[18] I. H. Lee, I. H. Choi, C. R. Lee, S. K. Noh, Appl. Phys. Lett. 71 (1997), 1359.

[19] P. Gay, P. B. Hirsch, A. Kelly, Acta Met. 1 (1953), 315.

[20] M. J. Hordon, B. L. Averbach, Acta Met. 9 (1961), 237.

[21] J. E. Ayers, J, Cryst. Growth, 135 (1994), 71.

[22] B. Heying, E. J. Tarsa, C. R. Elsass, P. Fini, S. P. DenBaars, J. S. Speck, J. Appl. Phys. 85 (1999), 6470.

[23] Y. Takehara, M. Yoshimoto, W. Huang, J. Saraie, K. Oe, A. Chayahara, Y. Horino, Jpn. J. Appl. Phys. 45 (2006), 67.

[24] S. Tixier, M. Adamcyk, T. Tiedje, S. Francoeur, A. Mascarenhas, P. Wei, F. Schiettekatte, Appl. Phys. Lett. 82 (2003), 2245.

[25] M. Yoshimoto, S. Murata, A. Chayahara, Y. Horino, J. Saraie, K. Oe, Jpn. J. Appl. Phys. 42 (2003), L1235.

[26] K. Oe, J. Cryst. Growth 237–239 (2002), 1481.

[27] K. Oe, Jpn. J. Appl. Phys. 41 (2002), 2801.

[28] K. Oe, H. Okamoto, Jpn. J. Appl. Phys. 37 (1998), L1283.

[29] A. Janotti, S. -H. Wei, S. B. Zhang, Phys. Rev. B 65 (2002), 115203.

[30] G. Ciatto, E. C. Young, F. Glas, J. Chen, R. A. Mori, T. Tiedje, Phy. Rev. B, 78 (2008), 35325.

[31] N. A. El-Masry, E. L. Piner, S. X. Liu, S. M. Bedair, Appl. Phys. Lett. 72 (1998), 40.

[32] S. Pereira, M. R. Correia, E. Pereira, P. O'Donnell, E. Aves, A. D. Sequeira, N. Franco, Appl. Phys. Lett. 79 (2001), 1432.

[33] P. Van der Sluis, J. Phys. D: Appl. Phys. 26 (1993), A188–A191.